PCCP

Accepted Manuscript

ROYAL SOCIETY OF CHEMISTRY

www.rsc.org/pccp

PCCP

PAPER

Nanostructured Ir-supported on Ti_4O_7 as cost effective anode for proton exchange membrane (PEM) electrolyzers†

Received 00th January 20xx,
Accepted 00th January 20xx

DOI: 10.1039/x0xx00000x

www.rsc.org/

Li Wang,[a] Philipp Lettenmeier,[a] Ute Golla-Schindler,[b] Pawel Gazdzicki,[a] Natalia A. Cañas,[a] Tobias Morawietz,[c] Renate Hiesgen,[c] S. Schwan Hosseiny,[a] Aldo S. Gago*,[a] and K. Andreas Friedrich[a,d]

PEM water electrolysis has recently emerged as one of the most promising technologies for large H_2 production from temporal surplus of renewable electricity, yet it is expensive partly due to the use of large amounts of Ir present in the anode. Here we report the development and characterization of a cost effective catalyst, which consists of metallic Ir nanoparticles supported on commercial Ti_4O_7. The catalyst is synthetized by reducing $IrCl_3$ with $NaBH_4$ in a suspension containing Ti_4O_7, cetyltrimethylammonium bromide (CTAB) and anhydrous ethanol. No thermal treatment was applied afterwards in order to preserve the high conductivity of Ti_4O_7 and metallic properties of Ir. Electron microscopy images show an uniform distribution of mostly single Ir particles covering the electro-ceramic support, although some agglomerates are still present. X-ray diffraction (XRD) analysis reveals a cubic face centered structure of the Ir nanoparticles with a crystallite size of ca. 1.8 nm. According to X-ray photoelectron spectroscopy (XPS), the ratio of metallic Ir and Ir-oxide, identified as Ir^{3+}, is 3:1 after the removal of surface contaminations. Other surface properties such as primary particle size distribution and surface potential were determined by atomic force microscopy (AFM). Cyclic and linear voltammetry was conducted to study the electrochemical surface and kinetics of Ir-black and Ir/Ti_4O_7. The developed catalyst outperforms commercial Ir-black in terms of activity for the oxygen evolution reaction (OER) in acid medium by a factor of four, measured at 0.25 V overpotential and room temperature. In general, the Ir/Ti_4O_7 catalyst exhibits improved kinetics and higher turnover frequency (TOF) compared to Ir-black. The developed Ir/Ti_4O_7 catalyst allows reducing the precious metal loading in the anode of a PEM electrolyzer by taking advantage of the use of an electro-ceramic support.

1. Introduction

Hydrogen can be used as an energy vector when produced from renewable energies such as solar or wind by using water electrolysis systems.[1] Commercially, hydrogen can be electrochemically produced by alkaline and PEM electrolysis. At present, the cost of the latter is almost twice the cost of the alkaline one.[2] However, PEM electrolyzers have the main advantage that they can be operated at much higher current densities than alkaline, thus an investment cost reduction is expected in the future.[3] One drawback of the PEM technology is that it requires the use of expensive precious group metals (PGM) electro-catalysts such as Ir and Pt in the anode and cathode, respectively. In particular, the anode requires a high loading of the scarce Ir metal of 2 – 4 mg cm^{-2},[4] because of the sluggish kinetics for the OER and high overpotential in the anode side.[5,6] Moreover, the electrochemical reaction mechanism is considered complex and high energy consuming.[7] Nanostructured RuO_2 and IrO_2 are the most active catalysts for OER in acid media.[6,8,9] While RuO_2 is much more active and cheaper than IrO_2, the stability is rather poor at high over-potentials leading to leaching of poisonous Ru^{4+}.[10] Several methods have been investigated in the last few years in order to address this challenge. One strategy is the optimization of the electrode design. In this context, Debe *et al.* developed an unsupported Ir-based anode with nanostructured thin film (NSTF) technique, achieving a comparable performance as commercial baseline but at 8 times lower Ir loading.[11]

Another way for reducing the amount of PGM is by using supporting materials, which is a common way in developing PEM fuel cell catalysts.[12,13] However, due to the operation of PEM electrolyzers at 2 V (nominal condition) or higher, the standard fuel cell catalyst supports such as carbon, are oxidized to CO_2.[14] Consequently, semi-conductive ceramics such as TiC [15] and TiO_2 [16] and conductive SnO_2 doped with Sb^{5+} [17] (ATO) or F^- [18] have been evaluated. Recent work by Strasser and co-workers were able to produce Ir/ATO with OER activities up to 70 A g_{Ir}^{-1} at an overpotential of 280 mV and 25

[a] Institute of Engineering Thermodynamics, German Aerospace Center, Pfaffenwaldring 38-40, Stuttgart, 70569, Germany. *E-mail address: aldo.gago@dlr.de; Fax: +49 711 6862-747; Tel.: +49 711 6862-8090
[b] Group of Electron Microscopy of Materials Science, Central Facility for Electron Microscopy, University of Ulm, 89081 Ulm, Germany
[c] University of Applied Sciences Esslingen, Dep. of Basic Science, Kanalstrasse 33, Esslingen, 73728, Germany
[d] Institute of Energy Storage, University of Stuttgart, Stuttgart, 70550, Germany

† Supporting information (SI) available with Rietveld analysis, additional AFM, XPS and calculation of active sites. See DOI: 10.1039/x0xx00000x

°C.[19,20] One alternative to ATO is to use Magnéli phases of TiO_2 or sub-oxides such as Ti_5O_9, Ti_4O_7 or a mixture of these, also know under the commercial name Ebonex®. These suboxides are highly conductive and corrosion resistant in acidic media under high overpotentials.[21] For this reason, these materials have been used in the cathode of PEM fuel cells [22,23] and more recently in cathode side of aprotic Li-O_2 batteries [24] and Li-S batteries.[25] In the PEM electrolysis field, Chen et al. reported an amelioration for the OER in acidic medium when using Ti_4O_7 as support of Ir-based catalysts.[26] Siracusano *et al.* reported as-well a significant improvement in the performance of a PEM electrolyzer anode, which contained a physical mixture of IrO_2 and Ti_4O_7.[27] In many ways Ti_4O_7 is more suitable as OER catalyst support than the popular ATO. For example, conductivities up to 10^3 S cm^{-1} at room temperature [21,28,29] were reported for Ti_4O_7 compared to ca. 0.3 S cm^{-1} for mesoporous ATO.[30] Furthermore, commercial Ti_4O_7 (Changsha PuRong, May 2015) can be mass-produced from TiO_2 with half of the production costs compared to ATO (Sigma-Aldrich, May 2015) with similar particle size. However, other important properties of Ir/Ti_4O_7 for electrolysis need to be clarified, in particular the improvement in kinetics and electrochemical surface reactions, long term stability under an accelerated stress test (AST) protocol, the effect of increasing BET surface area, bubble detachment efficiency, and hydrophilic properties at the nanoscale. In this work, we report the synthesis, physical and electrochemical characterization of nanostructured Ir- supported on commercial Ti_4O_7 as anode of PEM electrolyzers.

2. Experimental

2.1. Synthesis of Ir/Ti_4O_7 catalyst

Iridium supported on Ti_4O_7 (Ir/Ti_4O_7) catalyst was prepared via conventional sodium borohydride reduction method in anhydrous ethanol at room temperature. All chemical precursors were calculated for obtaining a loading of Ir on the Ti_4O_7 support of 30 wt. %. The synthesis procedure is schematized in Fig. 1. In short, 1.17 g cetyltrimethylammonium bromide (CTAB, Merck Millipore) and 0.1125 g Ti_4O_7 (Changsha Purong chemical engineering inc.) were dispersed in 120 mL anhydrous ethanol (VWR Chemicals) and stirred for 30 minutes in a three-neck round-bottom flask. An iridium solution composed of 0.0749 g iridium (III) chloride hydrate ($IrCl_3 \cdot xH_2O$, 99.9 %, Alfa Aesar) and 50 mL anhydrous ethanol was then added to Ti_4O_7 dispersion and stirred for 4 hours. The reduction of the Ir^{3+} took place by adding 114 mg $NaBH_4$ (VWR Chemicals) dissolved in 20 mL anhydrous ethanol at a rate of 2 mL min^{-1} under vigorous stirring. The reaction mixture was kept at this condition for 4 hours. All the procedures described above were carried out under argon atmosphere. The synthetized powder was filtered and washed several times with abundant pure ethanol. Finally, the collected powder was dried at 40 °C overnight.

2.2. Physical characterization

2.2.1. X-ray diffraction

X-ray diffraction data were collected on the Ir/Ti_4O_7 catalyst using a D8 Discover GADDS diffractometer with VÅNTEC-2000 areal detector. The X-ray source (Cu-Kα) consisted of a tuned monochromatic and parallel X-ray beam (accelerating voltage: 45 kV, tube current: 0.650 mA). The samples were measured on reflection mode in four frames with $\theta_1 = \theta_2$ (180 s per frame) and a step size of $2\theta = 23°$ (first frame $\theta = 12°$). The XRD spectrum of synthetized Ir powder was analyzed using the Topas program (Bruker AXS, version 5). For the Rietveld analysis, the cubic face centered structure was used for the fitting of Ir (space group: Fm-3m, CIF: 1512514, Crystallography Open Database). For the background, a polynomial background function of 3rd order was considered.

2.2.2. X-ray photoelectron spectroscopy

A Thermo Scientific ESCALAB 250 ultra-high vacuum (1 x 10^{-9}

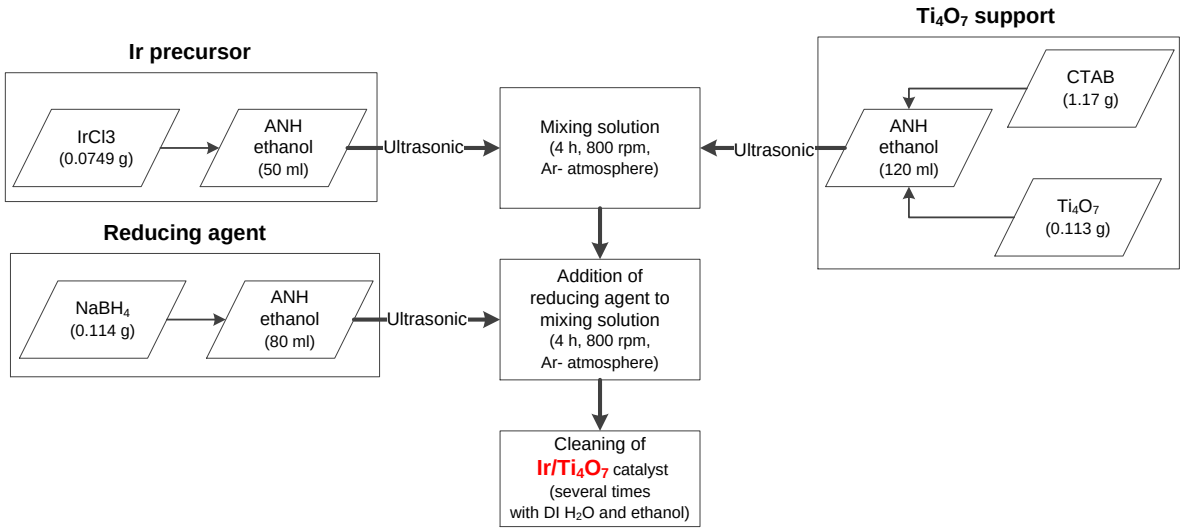

Fig. 1. Scheme of the synthesis procedure for 30 wt% Ir/Ti_4O_7 catalyst. DI = deionized water, ANH = anhydrous , CTAB = cetyltrimethylammonium bromide.

mbar base pressure) facility was used for XPS experiments. The depth profiles were conducted by means of subsequent Ar^+-sputtering and XPS analysis. The Ar^+ -sputtering was performed with a Thermo EX05 ion gun under the following conditions: 2 x 10^{-8} mbar Ar partial pressure; 2 kV acceleration voltage and 10 mA emission current, yielding an Ar^+ current of 4.4 µA at an area of 3 x 4 mm^2 (current density j_{Ar} = 0.22 µA/mm^2). For XPS measurements an Al Kα X-ray source (Thermo XR4) and a small area lens mode (0.8 mm^2) were chosen to ensure that the measuring spot was entirely within the sputtering crater. The atomic concentrations of elements in the samples were quantified using peak integrals and sensitivity factors provided by Thermo Scientific. For peak background correction a Shirley function was used. The sputtering yields are not calibrated for this material and hence, the depth profiles are plotted as function of sputter time only. To facilitate the comparison of our results with results of other groups we measured the sputter yield of Ta_2O_5/Ta sputtering reference samples with defined thickness of the Ta_2O_5 layers: for the sputter conditions used in this paper the sputter yield of the reference material corresponds to 0.12 nm s^{-1}. All XPS experiments were performed at room temperature and evaluated by the Thermo Scientific Avantage software. The powders were pressed into pellets to avoid charging of the powder samples during the experiments between individual grains. For depth profiling of the catalyst layers droplets of the catalyst ink have been deposited on a gold foil.

2.2.3. Atomic force and electron microscopy

The morphology of samples was observed using scanning electron microscopy (SEM, Zeiss ULTRA plus with Charge Compensation). The images were recorded based on backscattered electrons (BE) with the accelerating voltage of 1 kV. Energy-dispersive X-ray spectroscopy (EDX), which was combined in the SEM, was used to analyze the element composition of catalyst. The SEM was equipped with an XFlash 5010 detector (Bruker Corp.) for EDX analysis and the detector had an energy resolution of 123 eV at Mn Kα.

For AFM investigation, a Bruker Multimode 8 AFM (Karlsruhe, Germany) equipped with a Nanoscope V controller, a closed loop scanner with open loop Z-axis (nPoint, USA), an open loop EVLR scanner (Bruker Corp.), quantitative nano-mechanical tapping Mode (QNM™, Bruker Corp.), PeakForce Kelvin probe force microscopy (PF-KPFM, Bruker Corp.), and for current measurements, a lock-in current amplifier (PeakForce-TUNA™, Bruker Corp.) was used. The current measurements were performed with PtIr coated tips (PPP-NCHPt, 42 N/m; Nanosensors). In the QNM™ mode, mechanical properties are retrieved from the force-separation curve simultaneously to the height information. Thereby, adhesion force, stiffness, deformation, and energy dissipation mappings are recorded as reported elsewhere.[31] In PF-KPFM mode, the surface potential and the mechanical properties are measured alternatingly, with the tip lifted with constant distance above the surface during the potential measurements. The potential is retrieved via a nulling method.[32,33] The measured values are always the contact potential difference (CPD) to the Si AFM probe. For the PF-KPFM measurements, PFQNE-AL probes (Bruker) with a highly doped silicone tip on a nitride lever, a resonance frequency of 200-400 kHz, and a spring constant of 0.4-1.2 N/m were used. For high sensitivity, the lift height was set as low as possible without getting artefacts. In order to exclude a difference caused by change of the AFM probe, all measurements were performed with the same AFM probe. The sample was fixed with conductive tape to the AFM magnetic steel disk sample holder and was measured at ambient conditions.

Transmission electron microscopy (TEM) was performed using a Philips CM20 aligned for an accelerating voltage of 200kV equipped with a LaB6 cathode and a Keen View SIS camera. The sample material was directly dispersed on a free supporting lacey-carbon film (Plano) and the image data processing was performed by using Digital Micrograph from Gatan.

2.3. Electrochemical characterization

2.3.1. Electrode preparation

For the preparation of the catalytic ink, 10 mg sample was ultrasonically dispersed in 1.25 mL ultra-pure water (AlfaAesar) together with 0.25 mL Nafion® perfluorinated resin solution (5 wt. % in lower aliphatic alcohols and water, Sigma-Aldrich) to obtain a homogeneous suspension. Subsequently, 20 µL of the suspension was pipetted onto the surface of a ceramic shrouded glassy carbon rotating disk electrode (GC-RDE, 1 cm^2, Peter Schrems Elektroniklabor), which makes the implementation for temperature dependent measurements up to 70 °C. Prior the catalyst deposition, the GC-RDE was polished with alumina suspension (Buehler) until mirror-like finishing and ultrasonically cleaned, first in deionized water and then in pure ethanol. Once coated, the GC-RDE was dried at room temperature under Ar flow.

2.3.2. Electrochemical measurements

Cyclic voltammetry (CV) and linear scan voltammetry (LSV) were carried out in a three-electrode cell, in which GC-RDE was employed as working electrode. A Pt foil and a reversible hydrogen electrode (RHE, Gaskatel) were used as counter and reference electrode, respectively. All the electrochemical measurements were performed using an Autolab PGSTAT12 potentiostat. The OER measurements were performed from 1 to 1.6 V *vs.* RHE at a scan rate of 5 mV s^{-1} and a rotation speed of 2500 rpm with temperatures ranging from 25 up to 70 °C. The scan rate was kept sufficiently slow to decrease as much as possible the capacitance contribution to the measured current density. Before testing, pure Ar (purity 5.0, Linde) was bubbled into the electrolyte (0.5 M H_2SO_4 solution, VWR chemicals) for 30 minutes. All electrochemical measurements were corrected for the ohmic drop, which was determined by electrochemical impedance spectroscopy (EIS) using a module (Zahner IM6s) that generates an AC signal at a frequency of 5 x 10^4 Hz. Ir-black (Umicore) was used as reference OER catalyst for comparison purposes.

In addition, samples for AFM analysis after electrochemical measurements were prepared on GC plates of 1.8 x 1.8 cm^2

(AlfaAesar). Once the Ir/Ti_4O_7 catalyst ink was deposited on 1 cm^2 and dried, 200 cycles of CV were performed in O_2-saturated 0.5 M H_2SO_4 without rotation. Measurements were carried out at 25 °C with a sweep rate of 20 mV s^{-1}.

3. Results and discussion

3.1. Morphology and structure properties

SEM and TEM

The morphology of the Ir/Ti_4O_7 catalyst was studied with electron microscopy techniques, namely SEM and TEM. The loading of Ir on Ti_4O_7 was determined by EDX analysis in two ways (see supporting information) and it was found to be 24.2 ± 0.8 wt. %, indicating that not all the $IrCl_3$ was reduced during the synthesis procedure, in spite of the addition of $NaBH_4$ in excess. The unreacted $IrCl_3$ was dissolved through the repeated steps of washing with ethanol and water. SEM images were recorded with the energy selective backscattered (ESB) detector in order to enhance the compositional contrast between the Ir and the Ti_4O_7. One can observe in the low magnification micrograph of Fig. 2a, that the surface is quite bright indicating the presence of metallic Ir on most of the surface of Ti_4O_7. The dispersion of a metal phase depends significantly on the surface area of support. Brunauer–Emmett–Teller (BET) surface area measurements showed a specific surface area 8.04 m^2 g^{-1} for Ti_4O_7 powder. After the deposition of nano-sized Ir particles on Ti_4O_7, the BET surface increased to 38.03 m^2 g^{-1}. An image with higher magnification (Fig. 2b) clearly reveals that the Ir agglomerates are uniformly dispersed on the ceramic particles, which have irregular shape and are much darker than the precious metal. Interestingly, some very small agglomerates or even single nanoparticles scattered on Ti_4O_7 are visible as well. These particles can be noticed in Fig. 2b as tiny bright spots laying on the ceramic particles. Fig. 2c presents an overview TEM image of Ir/Ti_4O_7 catalysts. It shows Ir clusters (dashed circle) attached to the ceramic, which are not distributed homogeneously and seem to be quite scarce. The TEM image with increased magnification (Fig. 2d) confirms the presence of single Ir particles of ca. 2 nm in diameter and small agglomerates of less than 10 nm deposited on the Ti_4O_7 surface.

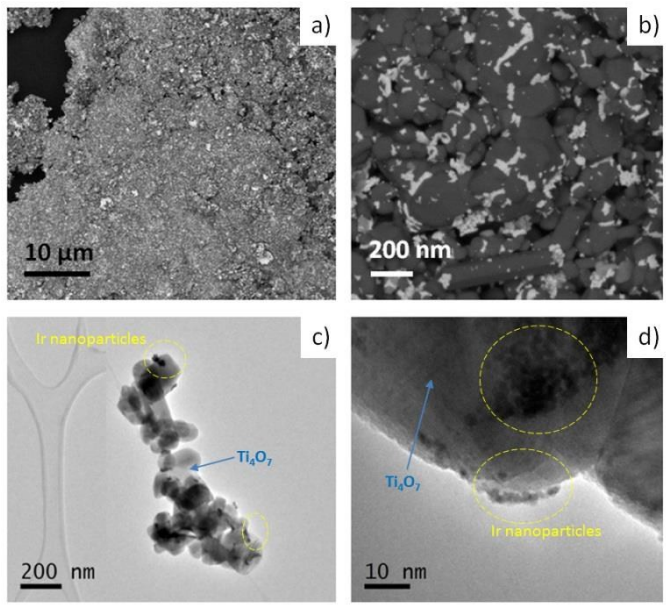

Fig. 3 (a) Low and (b) high magnification SEM images of Ir/Ti_4O_7 catalyst taken with backscattered electrons. The corresponding low and high resolution TEM images are shown in (c) and (d). Some agglomerates of Ir nanoparticles deposited on Ti_4O_7 are indicated with dashed yellow circles.

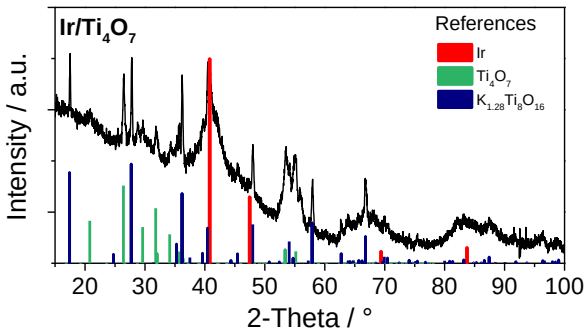

Fig. 2. X-ray diffraction pattern of Ir/Ti_4O_7 sample. References were taken from ICDD database (PDF): Ir: 03-065-1686, Ti_4O_7: 01-071-1428, $K_{1.28}Ti_8O_{16}$: 01-084-2058, $IrCl_3$: 00-001-0188.

3.1.2. XRD

The structure the Ir/Ti_4O_7 sample and the lattice parameters of Ir were determined by Rietveld analysis. The XRD pattern of Ir/Ti_4O_7 is presented in Fig. 3. It shows four main broad peaks corresponding to the cubic face centered structure of Ir (space group: Fm-3m). In Table 1, the crystalline properties of the Ir phase calculated with Rietveld analysis are summarized. The lattice parameters are similar as estimated by Wychoff,[34] and by Owen and Yates.[35] The crystallite size is ~1.8 nm as it can also be observed in the TEM images. The support material is composed of a mixture of Ti_4O_7 and $K_{1.28}Ti_8O_{16}$; the respectively mean crystallite size was 9.39 ± 0.19 nm and 150 ± 20 nm. The Rietveld refinement results and the comparison of measured and calculated spectra are shown in Fig. S1.

3.1.3. XPS

XPS spectra of the Ir 4f signal of freshly prepared Ir/Ti_4O_7 nano-powder after 0 s and 26 s of sputtering are presented in Fig.

Table 1. Structural parameters of Ir/Ti_4O_7 sample obtained from Rietveld refinement analysis. Detailed information is shown in Fig. S1 of supporting information.

Property	Ir
Structure	Cubic, face centered
Space group	Fm-3m
a (Å)	3.8284 (14)
Cell Volume (Å^3)	56.11 (6)
Crystallite size (nm)	1.78 (2)
Crystal density (g cm^{-3})	22.75 (3)
Cif file[a]	1512514

[a]Crystallography Open Database (http://www.crystallography.net/)

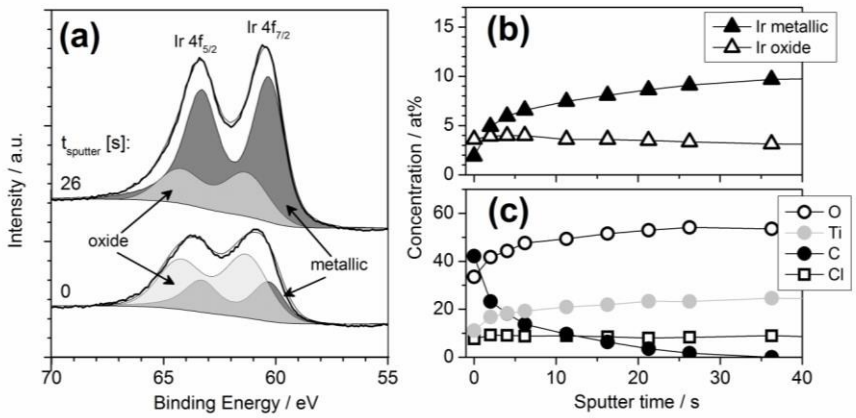

Fig. 4. XPS analysis showing (a) detailed Ir 4f spectra of Ir/Ti_4O_7, (b -c) a concentration profile of elements occurring in Ir/Ti_4O_7.

4a, along with the fits of the metallic and oxide components. The oxide species has been determined by fitting the first level spectrum (0 s) using the metallic reference (Ir black) and a synthetic doublet of symmetric peaks with 3 eV separation and a fixed height and width ratio. The outcome of the fit is an oxide species with the Ir $4f_{7/2}$ level located at 61.4 eV, which has been used to fit the Ir 4f spectra of all other levels of the XPS depth profile. According to a binding energy shift of -1 eV between the Ir-metallic peaks and the Ir-oxide the oxide species is very likely Ir^{3+}.[36] The concentration profiles of the metallic (Ir^0) and oxide Ir species (Ir^{3+}) as well as of other occurring elements (O, Ti, C, Cl) are summarized in Fig. 4b and Fig. 4c, respectively. Apparently, the low initial concentration of Ir, Ti and O is due to a contamination by surface carbon, which concentration becomes reduced down to virtually zero after ~30 s sputtering. Moreover, at the surface the concentration of Ir oxide is about twice the concentration of the metallic Ir component. Upon sputtering, the concentration of Ir^0 increases from 2 at% to about 10 at% while the concentration of Ir^{3+} remains largely constant; after 50 s sputtering the ratio Ir^0:Ir^{3+} = 3, i.e. the fraction of Ir oxide is substantial. Note that the constant Cl concentration of ~8 at% is due to the synthesis process of the sample. The un-reduced Ir^{3+} observed in XPS is associated with impurities of $IrCl_3$ (less than 2 wt%), which was used as Ir precursor of the Ir/Ti_4O_7 synthesis and could not be removed after the cleaning process. It is very unlikely the impurity $IrCl_3$ will play a role in the OER as it is removed from the surface of the catalyst layer after electrochemical oxidation at high potentials.

Finally, we do not observe a shift between Ir 4f peaks in Ir/Ti_4O_7 and Ir-black as it has been reported for Pt/Ti_4O_7 [23] and Pt/TiO_2,[37] so we do not have any indication for strong metal-support interaction.

From XPS spectra of pristine Ir/Ti_4O_7 based catalyst layers (prepared with Nafion as ionomer) as well as after electrochemical treatment is concluded that the thickness of the surface Ir-oxide layer slightly increases by ~30% after the electrochemical test (see supporting Information).

3.1.4. AFM on pristine materials

The topography measurements of the three different materials are given in Fig. 5. In Fig. 5a, the topography of Ir/Ti_4O_7 is shown and larger particles of the Magnéli phase can be clearly observed as well as the smaller Ir agglomerates. Fig. 5b shows the topography image of Ir black. On the topography image of the Ti_4O_7 coated sample (Fig. 5c) only larger crystals of Ti_4O_7 are visible.

The size of single Ir nanoparticles or smaller agglomerates on the Ti_4O_7 support measured by AFM are slightly higher than by XRD, but might be overestimated in the image due to convolution of tip and particle geometry. At higher magnification, given in Fig. 6a and Fig. 6b, Ir agglomerates are

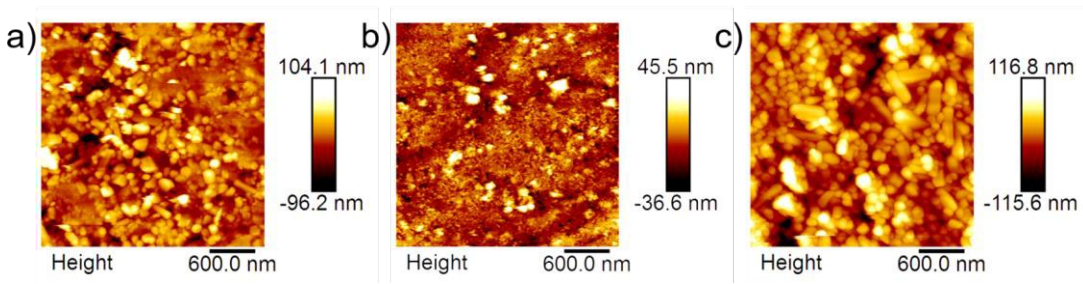

Fig. 5. Topography of the pellet samples: (a) Ir/Ti_4O_7, (b) Ir-black, and (c) Ti_4O_7.

Table 2. Results of a Gaussian fit of the AFM surface potential distribution measurements.

	xc / mV	A / mv²	w / mV
Ir black	721.65 ± 0.09	131.4 ± 0.6	41.6 ± 0.2
Ti_4O_7	78.5 ± 0.6	167 ± 2	122 ± 2
Ir/ Ti_4O_7	254.9 ± 0.7	153 ± 2	176 ± 2

visible on the Ti_4O_7 support, identified by their lower adhesion. This can be noticed in the adhesion image shown in Fig. 6c and Fig. 6d, from which the Ir nanoparticles (yellow dashed circles) and the Ti_4O_7 support can clearly be distinguished.

A comparison of the surface potential measured on the different samples by PF-KPFM is shown in Fig. 6e. The potential values at the peaks of the curves, fitted using a Gaussian distribution, are given in Table 2 along with the standard error. A shift in the potential from pure Ti_4O_7 to Ir/Ti_4O_7 of approximately 180 mV is associated to the Ir particles deposited on the Ti_4O_7 support. The much higher surface potential of pure Ir-black with 720 mV differs significantly from the potential of the mixed catalyst. A

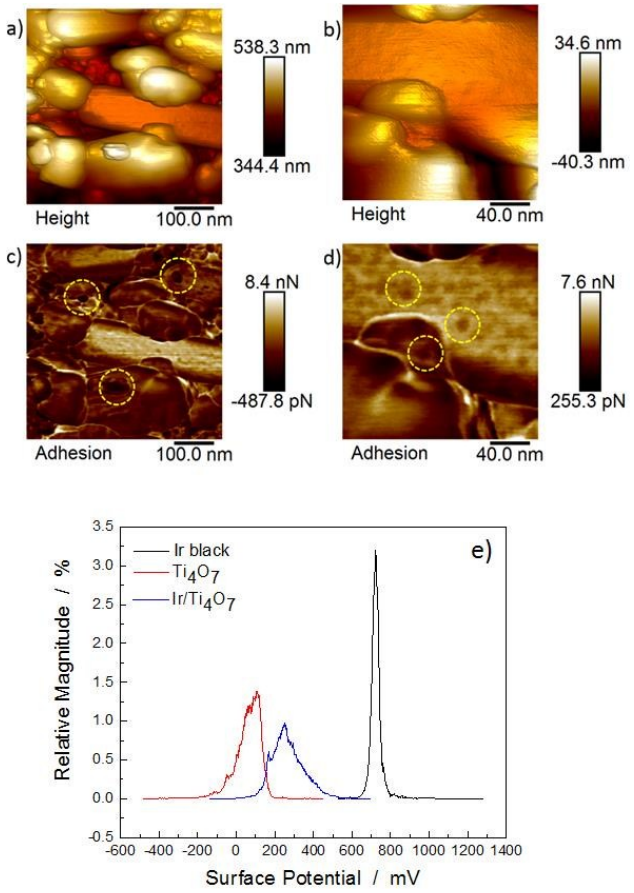

Fig. 6. Higher magnification topography image (a) and zoomed-in topography image (b) of Ir/Ti_4O_7; the corresponding adhesion image and zoomed-in adhesion image are shown in (c) and (d), on which Ir agglomerates on Ti_4O_7 are marked with yellow cycles; (e) the relative frequency of surface potential values of Ir Black, Ti_4O_7 and Ir/Ti_4O_7.

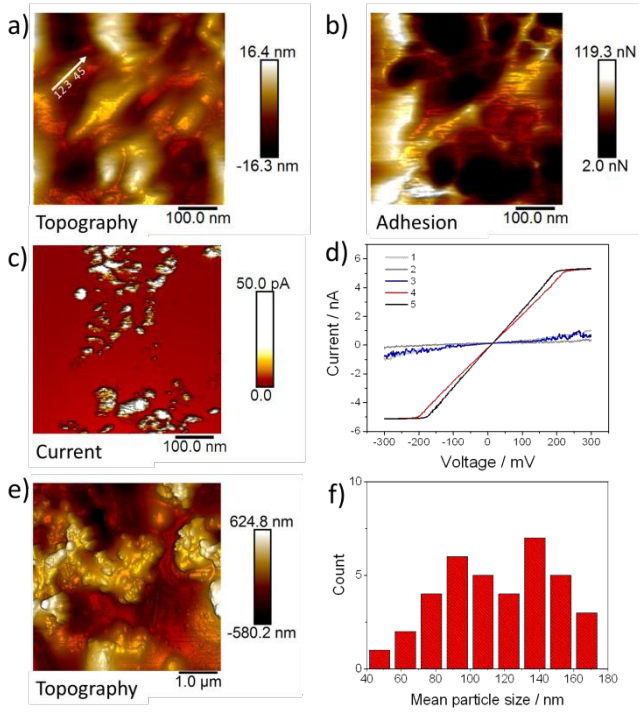

Fig. 7. AFM topography image (a) and the corresponding adhesion image (b) of Ir/Ti_4O_7 coated GC electrode; (c) shows the current measurement at the same position as (a); (d) I(V) curves along the white line on (a); zoomed-out topography image (e) and primary particle size distribution (f) of Ir/Ti_4O_7 on GC electrode.

decrease of the potential of the nano-particles is most likely caused by the mixed character of the catalyst. In addition, an adsorption of chloride ions on the catalyst that is known to lower the potential [38,39] has to be taken into account.

3.1.5. AFM on catalyst layers

200 cycles of CV between 1.0 and 1.6 V *vs.* RHE were carried out on Ir-black and Ir/Ti_4O_7 coated GC substrates in O_2-saturated 0.5 M H_2SO_4. The surface properties were studied before and after electrochemical treatment through ex-situ AFM measurements. Fig. 7a shows a topography image of the Ir/Ti_4O_7 catalyst layer. The adhesion of the AFM tip to the ionomer is higher than to the catalyst particles (Figure 7b). The dark spots on the particles in the adhesion image indicate that the ionomer covers the agglomerates and primary particles only partly.[40] Additionally, it was found for both catalysts that not all the particles are covered by the polymer, which has an impact on the surface potential and the conductivity. Fig. 7c and 7d show a current image and current-potential (I(V)) characteristics at different positions on an Ir/Ti_4O_7 electrode, respectively. The white line with numbers indicates the positions on the sample where the I(V) curves were measured. Higher resistance indicated thicker ionomer coverage of the particle. The corresponding broad primary particle size distribution, evaluated by measurements of particle size in the height image of Fig. 7e, is presented in Fig. 7f. An average primary particle size of 120 nm was determined for Ir/Ti_4O_7. In contrast, the average primary particle size of Ir-black is ca. 2.7

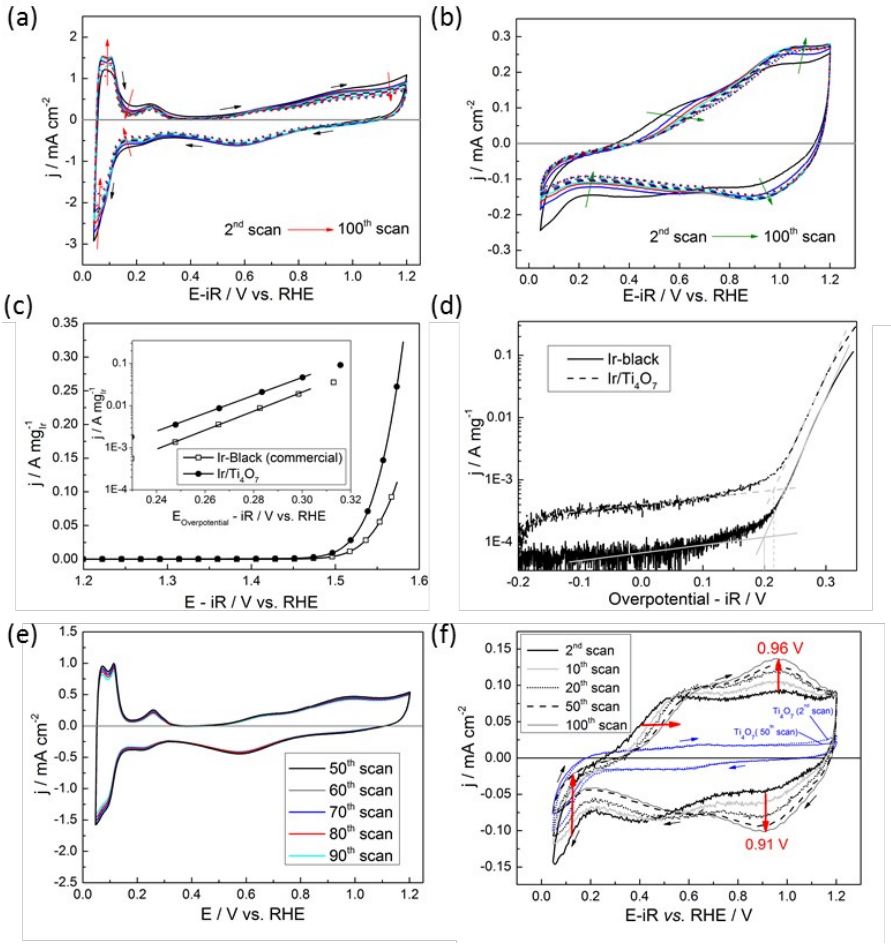

Fig. 8. Cyclic voltammetric curves of (a) Ir-black and (b) Ir/Ti_4O_7 deposited on the GC-RDE, measured at a sweep rate of 50 mV s^{-1}. (c) Mass activities of Ir-black and Ir/Ti_4O_7 catalysts for the OER measured at a sweep rate of 5 mV s^{-1} and rotation speed of 2500 rpm. The inset shows the corresponding Tafel slopes. A comparison of the j-E characteristics without normalization is shown in (d). Cyclic voltammetric curves of (e) Ir-black and (g) Ir/Ti_4O_7 after the OER measurements with different temperatures from 25 °C to 70 °C. All the experiments were carried out in Ar-saturated 0.5 M H_2SO_4 at 25 °C.

times larger (histogram not shown). After the electrochemical measurements, the average primary particle size shifted to 100 nm, most probably as result of displacement of Nafion ionomer that initially covered the particles during the gas evolving OER.[41]

3.2 Electrochemical surface properties and activity

3.2.1. Surface electrochemistry

In a PEM electrolyzer, the potential of the anode has to be raised more than 1.48 V (thermonuclear potential) in order to split water. Therefore, the Au-RDE is not suitable for studying Ir-based catalysts for OER in a half-cell as it forms unstable Au_2O_3 at 1.46 V *vs.* RHE,[42] posing difficulty for the analysis of kinetics and reproducibility (see supporting information). Consequently a ceramic RDE with GC disk was used for measurements when either the potential was higher than 1.48 V or the temperature of the electrolyte solution was varied. A number of CVs in deaerated 0.5 M H_2SO_4 were performed on the Ir-black and Ir/Ti_4O_7 coated GC-RDE prior to the OER measurements. The results CVs of Ir-black and Ir/Ti_4O_7 are presented in Fig. 8a and Fig. 8b, respectively.

First, the cyclic voltammetric curve of Ir-black is almost identical to the one presented in Fig. S5 (a). However, the peaks of the three characteristic zones of the CV, namely the hydrogen ionisation, double layer and oxide formation, are clearer and more defined. Second, in the case of Ir/Ti_4O_7, below 0.2 V *vs.* RHE the contribution to the cathodic currents of the H_{ads} peaks by the electro-ceramic support is very noticeable. It is also interesting that waves from the formation of $Ir(OH)_3$ and hydrous Ir^{4+} shift positively with each cycle. This result is similar to what it has been reported for Ir nanoparticles supported on carbon.[43]

3.2.2. Activity and kinetics

The OER mass activities of Ir-black and Ir/Ti_4O_7 were measured at different temperatures in order to study the kinetic behavior of the materials. The elemental analysis discussed in Section 3.1 revealed an Ir loading of ca. 25 wt. % on Ti_4O_7. Therefore, the PGM loading on the GC-RDE is about 33 μg_{Ir} cm^{-2}. This value was used for normalizing the mass activity of

Table 3. Kinetic parameters for OER on Ir/Ti_4O_7 and commercial Ir-black catalysts. The onset overpotential (η), Tafel slope (β), transfer coefficient (α) and exchange current density (j_o) are listed against temperature (T), for both materials.

	T / °C	η / V	β / mV dec^{-1}	α	j_o / 10^{-9}A mg_{Ir}^{-1}
Ir/Ti_4O_7	25	0.212	47.3	0.63	21
	30	0.211	46.6	0.65	19.5
	40	0.202	46.9	0.66	34.5
	50	0.196	46.7	0.69	52.0
	60	0.190	46.4	0.71	75.1
	70	0.184	47.4	0.72	140.2
Ir-black	25	0.198	43.1	0.69	2.5
	30	0.195	43.1	0.70	3
	40	0.185	43.2	0.72	5.8
	50	0.178	43.6	0.73	12.0
	60	0.169	43.9	0.75	22.8
	70	0.162	44.6	0.76	46.2

Ir/Ti_4O_7 after ohmic correction. Fig. 8c shows the current-potential characteristics of both catalysts in Ar-saturated 0.5 M H_2SO_4 at 25 °C and a sweep rate of 5 mV s^{-1}. At an overpotential of 0.25 V, the mass activity was measured to 4.2 and 1.6 A g_{Ir}^{-1} for supported and unsupported catalyst, respectively. This result shows that Ir/Ti_4O_7 has a better utilization of the PGM catalyst for the OER than commercial Ir-black. The electrochemical parameters obtained from the LSVs carried out at different temperatures are summarized in Table 3. One can observe in Fig. 8d that the overpotential (η) of Ir/Ti_4O_7 is shifted ca. 20 mV towards the positive and this value does not depend on temperature (see column 2 in Table 3). It is well known the dependence of the electric resistance of Ti_4O_7 bulk material such as pellet, layers, etc. with respect to the compactness.[44] The ohmic drop of Ti_4O_7 coated RDEs was measured with electrochemical impedance spectroscopy (EIS), but not difference in the obtained values was found. The Ti_4O_7 support definitely has influence in electrocatalytic properties of Ir/Ti_4O_7 (e.g. shift of the onset potential). The unsupported Ir produced by similar synthesis route [45] shows the same onset potential than Ir-black. However, at present there is no experimental evidence that the observed electrochemical behavior of Ir/Ti_4O_7 is due to the higher electronic resistance.

The Tafel slope (β) of Ir/Ti_4O_7 and Ir-black layers, in both cases, is between 40-60 mV which is normally accepted in the literature for non-compact layers [46–49] and demonstrates that both catalysts exhibit the similar rate-determining step for the OER. The observed Tafel slope does not contradict the OER mechanism proposed in the literature.[50,51] That is a one electron non-faradic step in which OH_{ads} surface species are rearranged via a surface reaction according to the following mechanism:

$$S+H_2O \rightarrow S\text{-}OH_{ads}{}^{*}+H^{+}+e^{-}, \quad (1)$$

$$S\text{-}OH_{ads}{}^{*} \rightarrow S\text{-}O_{ads}{}^{-}+H^{+}, \quad (2)$$

$$S\text{-}O_{ads}{}^{-} \rightarrow S\text{-}O_{ads}+e^{-}, \quad (3)$$

$$S\text{-}O_{ads}+S\text{-}O_{ads} \rightarrow O_2+2S, \quad (4)$$

where S represents the active site of the catalytic metal. The theoretical value of Tafel slope β of the Eq. (3) can be calculated using the relation $\beta = RT\ \ln 10 / (2\alpha) F$, where R is the gas constant (8.31 J K^{-1} mol^{-1}), α the transfer coefficient, T the absolute temperature and F the Faraday constant (9.65 x 10^4 C mol^{-1}). Thus β is ca. 47 mV dec^{-1} (at 80 °C) which is quite close to the measured values of 47.3 and 43.1 mV dec^{-1} for Ir/Ti_4O_7 and Ir-black, respectively. In recent years, it has been demonstrated that the difficult step in the water splitting process is the formation of hydroperoxide-type (OOH) species of metal surfaces that are partly-oxidized, according to deprotonation mechanism:[52,53]

$$H_2O + S\text{-}O_{ads} \rightarrow S\text{-}OOH_{ads} + H^{+}+e^{-}. \quad (5)$$

The formation of OOH_{ads} eventually leads to the evolution of molecular O_2, which proves that in fact other complex factors can affect the kinetic behaviour of the β in nanostructured and partly-oxidized catalysts such as Ir/Ti_4O_7 and Ir-black. Therefore, only in-situ spectroscopies and other sophisticated characterization techniques at the atomic level can really provide insight on the OER mechanism of the materials discussed herein.

A number of CVs were performed in deaerated 0.5 M H_2SO_4 in order to study the changes in the electrochemical surface of the materials after the OER measurements performed at different temperatures (from 25 °C to 70 °C). The results are summarized in Fig. 8e and Fig. 8f for Ir-black and Ir/Ti_4O_7, respectively. At first, we can observe in Fig. 8e that peaks from the triplet associated to H_{ads} in Ir-black are more defined compared to Fig. 8a. Moreover, the characteristic Ir-redox pairs are also more pronounced in these CVs than in the OER measurements. Notably, the redox pair of Ir^{3+}/Ir^{4+} of the Ir/Ti_4O_7 (Fig. 8f) can be easily distinguished showing how the absolute current density centered at ca. 0.9 V increases progressively with every cycle. Interestingly, the oxidation peak of Ir^{3+} in Ir/Ti_4O_7 is shifted positively more than 50 mV compared to the reduction peak of Ir^{4+}, while for Ir-black the difference is only about 10 mV (see Fig. S6, supporting information).

The larger shift on Ir/Ti_4O_7 can be attributed to the ceramic support, as it occurred for the OER onset potential.

4. Conclusions

The Ir/Ti_4O_7 anode catalyst is a promising material for reducing the precious metal loading in the PEM electrolyzer for large scale storage of renewables. In many ways the Ir/Ti_4O_7 catalyst is thermodynamically more efficient on a noble metal mass and an active site basis during the electrocatalytic oxygen evolution than commercial Ir-black. It has a higher OER activity, higher TOF on each active center, and better

utilization of the precious metal compared to Ir-black. In general it has improved kinetic properties, except for a slight shift in the water splitting onset potential, which is attributed to the ohmic drop from the lack of compactness of the catalyst layer. Even though this catalyst appears attractive as anode material for polymer electrolysis the structural and chemical complexity complicates the elucidation of the OER mechanism and the effect of using an electro-ceramic supports.

Acknowledgements

The authors acknowledge the German BMWi for financial support in the project No. 0325440A. The authors thank as well Anke Steinhilber (DLR) for further XPS analysis, Dr. Noriko Metzger-Sata (DLR) for BET measurements, and Dr. Rémi Costa (DLR) for helpful discussion on point of zero charge (PZC) measurements. The authors also acknowledge Dr. Jürgen Kraut (Hochschule Esslingen) for further EDX analysis.

Notes and references

1 A. Sternberg and A. Bardow, *Energy Environ. Sci.*, 2015, **8**, 389–400.
2 Fuel Cells and Hydrogen Joint Undertaking (FCH JU), *Commercialisation of energy storage in europe, Final Report*, March 2015, Page 52.
3 K. E. Ayers, E. B. Anderson, C. Capuano, B. Carter, L. Dalton, G. Hanlon, J. Manco and M. Niedzwiecki, *ECS Trans.*, 2010, **33**, 3–15.
4 M. Carmo, D. L. Fritz, J. Mergel and D. Stolten, *Int. J. Hydrogen Energy*, 2013, **38**, 4901–4934.
5 A. Marshall, B. Børresen, G. Hagen, M. Tsypkin and R. Tunold, *Energy*, 2007, **32**, 431–436.
6 Y. Lee, J. Suntivich, K. J. May, E. E. Perry and Y. Shao-Horn, *J. Phys. Chem. Lett.*, 2012, **3**, 399–404.
7 S. Park, Y. Shao, J. Liu and Y. Wang, *Energy Environ. Sci.*, 2012, **5**, 9331.
8 E. A. Paoli, F. Masini, R. Frydendal, D. Deiana, C. Schlaup, M. Malizia, T. W. Hansen, S. Horch, I. E. L. Stephens and I. Chorkendorff, *Chem. Sci.*, 2014, **00**, 1–7.
9 E. Fabbri, A. Habereder, K. Waltar, R. Kötz and T. J. Schmidt, *Catal. Sci. Technol.*, 2014, **4**, 3800–3821.
10 R. Kötz, S. Stucki, D. Scherson and D. M. Kolb, *J. Electroanal. Chem. Interfacial Electrochem.*, 1984, **172**, 211–219.
11 M. K. Debe, S. M. Hendricks, G. D. Vernstrom, M. Meyers, M. Brostrom, M. Stephens, Q. Chan, J. Willey, M. Hamden, C. K. Mittelsteadt, C. B. Capuano, K. E. Ayers and E. B. Anderson, *J. Electrochem. Soc.*, 2012, **159**, K165–K176.
12 S. Sharma and B. G. Pollet, *J. Power Sources*, 2012, **208**, 96–119.
13 Y. Shao, J. Liu, Y. Wang and Y. Lin, *J. Mater. Chem.*, 2009, **19**, 46–59.
14 T. Ioroi, Z. Siroma, N. Fujiwara, S. Yamazaki and K. Yasuda, *Electrochem. commun.*, 2005, **7**, 183–188.
15 L. Ma, S. Sui and Y. Zhai, *J. Power Sources*, 2008, **177**, 470–477.
16 R. E. Fuentes, J. Farell and J. W. Weidner, *Electrochem. Solid-State Lett.*, 2011, **14**, E5.
17 V. K. Puthiyapura, M. Mamlouk, S. Pasupathi, B. G. Pollet and K. Scott, *J. Power Sources*, 2014, **269**, 451–460.
18 K. Kadakia, M. K. Datta, P. H. Jampani, S. K. Park and P. N. Kumta, *J. Power Sources*, 2013, **222**, 313–317.
19 H.-S. Oh, H. N. Nong, T. Reier, M. Gliech and P. Strasser, *Chem. Sci.*, 2015, **00**, 1–8.
20 H. N. Nong, H.-S. Oh, T. Reier, E. Willinger, M.-G. Willinger, V. Petkov, D. Teschner and P. Strasser, *Angew. Chemie Int. Ed.*, 2015, **54**, 2975–2979.
21 F. C. Walsh and R. G. a. Wills, *Electrochim. Acta*, 2010, **55**, 6342–6351.
22 T. Ioroi, H. Senoh, S. Yamazaki, Z. Siroma, N. Fujiwara and K. Yasuda, *J. Electrochem. Soc.* , 2008, **155** , B321–B326.
23 C. Yao, F. Li, X. Li and D. Xia, *J. Mater. Chem.*, 2012, **22**, 16560–16565.
24 D. Kundu, R. Black, E. J. Berg and L. F. Nazar, *Energy Environ. Sci.*, 2015, **8**, 1292–1298.
25 X. Tao, J. Wang, Z. Ying, Q. Cai, G. Zheng, Y. Gan, H. Huang, Y. Xia, C. Liang, W. Zhang and Y. Cui, *Nano Lett.*, 2014, **14**, 5288–5294.
26 G. Chen, S. R. Bare and T. E. Mallouk, *J. Electrochem. Soc.*, 2002, **149**, A1092.
27 S. Siracusano, V. Baglio, C. D'Urso, V. Antonucci and A. S. Aricò, *Electrochim. Acta*, 2009, **54**, 6292–6299.
28 R. F. Bartholomew and D. R. Frankl, *Phys. Rev.*, 1969, **187**, 828–833.
29 T. Ioroi, H. Kageyama, T. Akita and K. Yasuda, *Phys. Chem. Chem. Phys.*, 2010, **12**, 7529–35.
30 H.-S. Oh, H. N. Nong and P. Strasser, *Adv. Funct. Mater.*, 2015, **25**, 1074–1081.
31 R. Hiesgen, S. Helmly, T. Morawietz, X.-Z. Yuan, H. Wang and K. A. Friedrich, *Electrochim. Acta*, 2013, **110**, 292–305.
32 M. Nonnenmacher, M. P. O'Boyle and H. K. Wickramasinghe, *Appl. Phys. Lett.*, 1991, **58**, 2921.
33 U. Zerweck, C. Loppacher, T. Otto, S. Grafström and L. M. Eng, *Phys. Rev. B*, 2005, **71**, 125424.
34 R. W. G. Wyckoff, *Cryst. Struct.*, 1963, 7–83.
35 E. A. Owen and E. L. Yates, *Philos. Mag.*, 1933, 472–488.
36 J. Augustynski, M. Koudelka, J. Sanchez and B. E. Conway, *J. Electroanal. Chem.*, 1984, **160**, 233–248.
37 A. Lewera, L. Timperman, A. Roguska and N. Alonso-Vante, *J. Phys. Chem. C*, 2011, **115**, 20153–20159.
38 G. Cabailh, C. R. Henry and C. Barth, *New J. Phys.*, 2012, **14**, 103037.
39 C. Ganzorig, K.-J. Kwak, K. Yagi and M. Fujihira, *Appl. Phys. Lett.*, 2001, **79**, 272.
40 R. Hiesgen, T. Morawietz, M. Handl, M. Corasaniti and K. A. Friedrich, *Electrochim. Acta*, 2015, **162**, 86–99.
41 F. M. Sapountzi, S. C. Divane, E. I. Papaioannou, S. Souentie and C. G. Vayenas, *J. Electroanal. Chem.*, 2011, **662**, 116–122.
42 L. D. Burke and P. F. Nugent, *Gold Bull*, 1997, **30**, 43–53.
43 T. Reier, M. Oezaslan and P. Strasser, *ACS Catal.*, 2012, **2**, 1765–1772.
44 P. C. S. Hayfield, *Development of a New Material-Monolithic Ti_4O_7 Ebonex@ Ceramic*, Royal Society of Chemistry, Cambridge, UK, 2002.

45 P. Lettenmeier, L. Wang, U. Golla-Schindler, P. Gazdzicki, N. A. Cañas, M. Handl, R. Hiesgen, S. S. Hosseiny, A. S. Gago and K. A. Friedrich, *Angew. Chemie*, 2015, DOI: 10.1002/ange.201507626.

46 A. Minguzzi, O. Lugaresi, E. Achilli, C. Locatelli, A. Vertova, P. Ghigna and S. Rondinini, *Chem. Sci.*, 2014, **5**, 3591.

47 G. Lodi, E. Sivieri, a Debattisti and S. Trasatti, *J. Appl. Electrochem.*, 1978, **8**, 135–143.

48 T. Audichon, E. Mayousse, T. W. Napporn, C. Morais, C. Comminges and K. B. Kokoh, *Electrochim. Acta*, 2014, **132**, 284–291.

49 A. K. M. Fazle Kibria and S. a. Tarafdar, *Int. J. Hydrogen Energy*, 2002, **27**, 879–884.

50 J. O. Bockris and T. Otagawa, *J. Phys. Chem.*, 1983, **87**, 2960–2971.

51 a. Damjanovic, a. Dey and J. O. Bockris, *J. Electrochem. Soc.*, 1966, **113**, 739.

52 J. Rossmeisl, a. Logadottir and J. K. Nørskov, *Chem. Phys.*, 2005, **319**, 178–184.

53 H. G. Sanchez Casalongue, M. L. Ng, S. Kaya, D. Friebel, H. Ogasawara and A. Nilsson, *Angew. Chemie*, 2014, **126**, 7297–7300.